



## Middle Eocene Climatic Optimum (MECO) and its imprint in the continental Escanilla Formation, Spain

Nikhil Sharma<sup>1</sup>, Jorge E. Spangenberg<sup>2</sup>, Thierry Adate<sup>3</sup>, Torsten Vennemann<sup>2</sup>, László Kocsis<sup>2</sup>,

Jean Vérité<sup>1,4</sup>, Luis Valero<sup>1,5</sup>, Sébastien Castelltort<sup>1</sup>

5 <sup>1</sup>Department of Earth Sciences, University of Geneva, Rue des Maraichers 13, 1205 Geneva, Switzerland

<sup>2</sup>Institute of Earth Surface Dynamics (IDYST), University of Lausanne, Géopolis, 1015 Lausanne, Switzerland


<sup>3</sup>Institute of Earth Sciences (ISTE), University of Lausanne, Géopolis, 1015 Lausanne, Switzerland

<sup>4</sup>LPG – Le Mans, UFR Sciences et Techniques, Université du Maine, 72089 Le Mans cedex 9, France

<sup>5</sup>Departament de Dinàmica de la Terra i l'Oceà, Facultat de Ciències de la Terra, Barcelona, 08028, Spain

10

Correspondence to: Nikhil Sharma ([nikhil.sharma@unige.ch](mailto:nikhil.sharma@unige.ch))

**Abstract.** The Middle Eocene Climatic Optimum (MECO) is a global warming event mainly described in the marine domain but less in the terrestrial domain. This study presents a comprehensive geochemical record of the  
15 MECO from the Escanilla Formation, a fluvial sedimentary succession in the southern Pyrenees, Spain, based on a suite of sampled paleosols, fluvial stromatolites and pedogenic nodules. Our multiproxy approach involves using carbon and oxygen stable isotope compositions to identify the regional preservation of the MECO, calculate chemical weathering intensity and identify the clay mineralogy of paleosols, as well as to estimate mean annual precipitation using temperature estimates based on clumped isotope compositions of carbonates. Results indicate  
20 that the Middle Eocene interval in the south central Pyrenees was characterized by low weathering rates under warm and arid climatic conditions. This is further supported by the presence of smectite, palygorskite, illite, and chlorite, which suggest seasonal rainfall but under generally dry conditions resulting in weak chemical weathering.   
Importantly, an isotopic excursion indicates a regional, terrestrial impact of the MECO, highlighting that fluvial sedimentary successions even in active foreland basins can represent particularly interesting terrestrial archives  
25 of past changes in global climate.

### 1 Introduction



The Middle Eocene Climatic Optimum (MECO) is a transient global warming event that occurred during the Bartonian (40.0 Ma) and represents a significant reversal in the long-term cooling trend of the Middle to Upper  
30 Eocene [Bohaty et al., 2009]. It is characterized by a distinct negative oxygen isotope excursion (OIE) of about 1 ‰ interpreted as a 3 to 6 °C rise in global ocean temperatures, and a subdued and spatially non-uniform negative carbon isotope excursion (CIE) in marine carbonates [e.g., Bohaty et al., 2009; Bijl et al., 2010; Henehan et al., 2020]. This lack of a distinct negative and robust CIE, a key diagnostic feature of earlier Cenozoic hyperthermals such as the Paleocene Eocene Thermal Maximum (PETM), its comparatively long duration (~500 Kyr), along  
35 with elevated pCO<sub>2</sub> levels sustained over a long period by a diminished silicate weathering feedback [van der Ploeg et al., 2018], points towards an instability in the long-term carbon cycle during the MECO [Sluijs et al., 2013]. In principle, elevated global temperatures and CO<sub>2</sub> levels are expected to be reflected in continental environments in the form of increased silicate weathering of exposed rocks. This process helps restore the climate through a drawdown of the atmospheric CO<sub>2</sub> level, associated with an intensified hydrological cycle [e.g., Sluijs  
40 et al., 2013; Methner et al., 2016; van der Ploeg et al., 2018].

While the MECO has been extensively identified in both onshore and offshore marine sedimentary sections [e.g., Jovane et al., 2007; Bohaty et al., 2009; Spofforth et al., 2010], only a few studies have identified it in terrestrial successions [e.g., Bosboom et al., 2014; Mulch et al., 2015; Methner et al., 2016]. Currently available data from the terrestrial realm suggests important regional differences in response to the MECO. For instance, Bosboom et  
45 al. (2014) discuss the onset of region-wide arid conditions in the Xining Basin, China, while Methner et al. (2016) predicted large temperature seasonality and an intensification of the hydrologic cycle in the continental interiors of north-western America. These regional differences highlight the need to further document records of the MECO in continental depositional systems to provide more constraints for understanding the dynamics of the climate and Earth's surface perturbations during that period.

To contribute to this issue, we document a new record in the Escanilla Formation (Fm), a fluvial sedimentary  
50 succession in the southern Pyrenees at Olson (Spain), using carbon stable isotope compositions ( $\delta^{13}\text{C}$ ) of paleosol organic matter to highlight the regional preservation of the MECO. We also measured the carbon and oxygen stable isotope ratios of carbonates in stromatolites, pedogenic nodules, and bulk paleosols to further examine the terrestrial MECO related changes in the carbon and water cycles. We calculated the weathering indices to quantify  
55 weathering intensity during the MECO, and reconstructed climatic conditions using mean annual precipitation estimates, carbonate clumped isotope thermometry, and clay mineralogy.



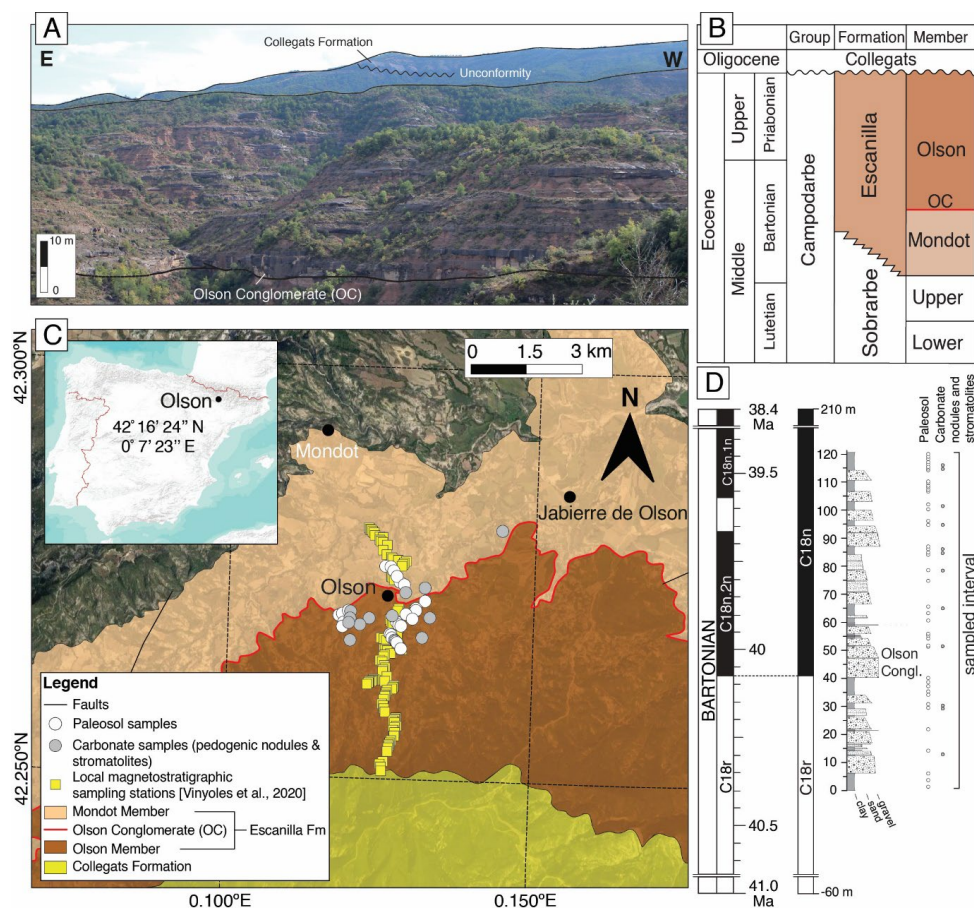
## 2 Study locality and age constraints

### 2.1 Escanilla Fm

60 The Escanilla Fm at Olson has a maximum thickness of 1000 m and is subdivided into the Mondot and Olson Members (Figs. 1B, 1C) [e.g., Labourdette and Jones, 2007]. At the transition of these two Members lies a basin-wide extending conglomeratic channel-complex, hereafter referred to as the Olson Conglomerate (OC), which is the interpreted stratigraphic expression of peak MECO warming in the Escanilla Fm based on available age constraints (Figs. 1B–1D). The Escanilla Fm predominantly consists of conglomeratic to sandy channel-fill  
65 deposits and their adjacent fine-grained floodplain/overbank deposits. These floodplain fines have been previously characterized as entisols, i.e., displaying a very low degree of pedogenesis over a limited period [Dreyer et al., 1992]. In addition, we document the presence of three pedogenic carbonate nodule horizons (Fig. 2C) and nine fluvial stromatolites preserved within the Escanilla floodplains (Figs. 2E–2G). Although fluvial stromatolites are common in the upper Palaeocene to Eocene fluvial deposits of Spain [Zamarreno et al., 1997], they had not been  
70 identified in the Escanilla Fm before (to our knowledge). These stromatolites have been preserved as elongated domes with an asymmetrical shape and have varying lengths from a few centimeters to a meter and from 15 – 60 cm in diameter. They have been interpreted as having formed as overbank deposits of fluvial channels with a preferential elongation presumably parallel to the flow direction [Zamarreno et al., 1997]. Within this context, a composite section of about 120 m was sampled for a suite of paleosol and carbonate (pedogenic nodules and  
75 stromatolites) samples, carefully avoiding all traces of modern pedogenesis. Locations of sampled sites and corresponding raw data from different analyses are provided in the Supplementary Material.

### 2.2 Age constraints

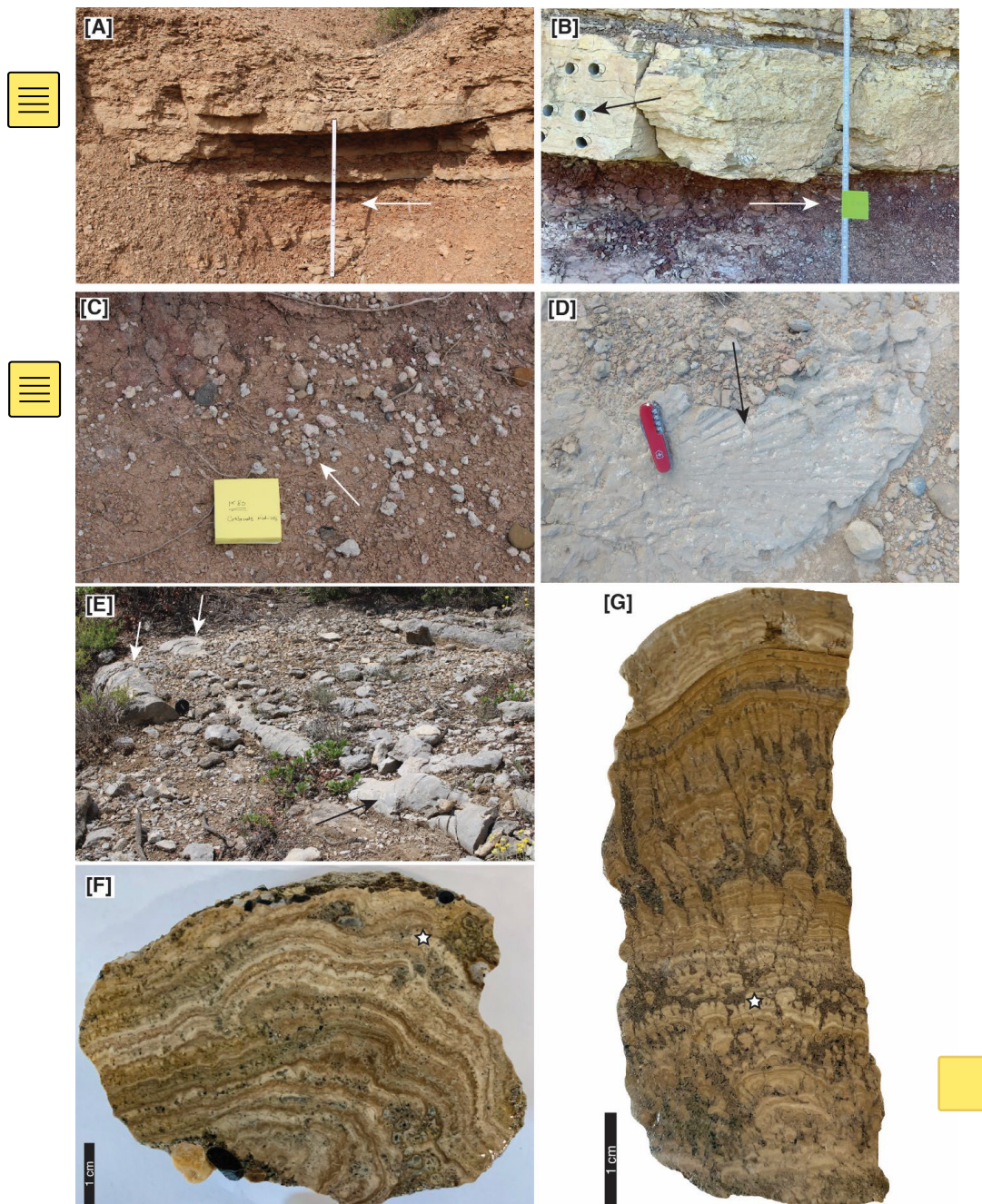
To compare our data relative to the target MECO isotope excursion from ODP site 738 [Bohaty et al. (2009)] and the Geomagnetic Polarity Time Scale (GPTS 2020), a first-order linear correlation between the base (at 40 m) and  
80 the top (at 210 m) of Chron C18n (magnetostratigraphic data of Vinyoles et al., 2020), and to the base of Chron C18n.2n and top of Chron C18n.1n on the Geomagnetic Polarity Time Scale (GPTS 2020) has been calculated (Fig. 1D) [Ogg 2020]. All data are presented relative to the thickness of the sampled Olson section accompanied by the local magnetostratigraphic interpretation of Vinyoles et al., (2020), linearly scaled to the GPTS 2020.



85 Figure 1 (A) Field image depicting the sampled Escanilla Fm. (B) Lithostratigraphic framework of the Escanilla Fm at Olson consists of two main Members – the Mondot and the Olson Member with the Olson sheet (red line) at the transition between the two Members. (C) Map showing the extent of the Escanilla Fm in northern Spain. Also shown is an inset map of Spain, indicating the village of Olson where the study was carried out. Map modified from [Labourdette and Jones \(2007\)](#). (D) Sampled composite section, with position of each collected sample, of the Escanilla Fm together with the local magnetostratigraphic interpretation by [Vinyoles et al. \(2020\)](#) correlated to the Geomagnetic Polarity Time Scale (GPTS 2020) [[Ogg, 2020](#)]. The thickest normal magnetozone C18n in the local magnetostratigraphic interpretation includes C18n.1n, C18n.1r, and C18n.2n.

90





95

Figure 2. (A, B) Typical sampled paleosols (indicated by white arrows) from the Escanilla Fm characterized as brownish-red mudstones that underwent minimal pedogenesis. Sample collected by Vinyoles et al., (2020) to test for the magnetic fabric of the sandstone has been indicated by a black arrow. (C) A sampled carbonate nodule level just above the OC. (D) A palm tree



leaf imprint found in the Escanilla Fm because of its radial appearance plausibly resembles the now extinct genus of palm *Sabalites* [Villalba-Breva et al., 2012] (E) Long, tubular stromatolites (marked by white arrows) as preserved in the floodplain. (F, G) Cross-section of stromatolite samples NS7 and NS1 respectively, showing the well preserved individual layering. The white stars indicate micro-drilling sites.

100

### 3 Material and methods

Analyses were carried out on a suite of sampled paleosols ( $N = 45$ ), stromatolites ( $n = 9$ ), and pedogenic nodules ( $n = 9$ ). Powders of bulk paleosol samples were prepared and analyzed for a suite of geochemical indicators, including total organic carbon (TOC) content, Rock-Eval parameters, organic carbon isotope compositions ( $\delta^{13}\text{C}_{\text{org}}$ ), carbonate carbon and oxygen isotopes ( $\delta^{13}\text{C}_{\text{carb}}$  and  $\delta^{18}\text{O}_{\text{carb}}$ ), major elements, and clay mineral assemblages. Stromatolite and pedogenic nodule powders were analyzed for  $\delta^{13}\text{C}_{\text{carb}}$  and  $\delta^{18}\text{O}_{\text{carb}}$  and clumped isotope compositions ( $\delta^{47}$  and  $\Delta_{47}$ ). We summarize the methods below, and details are available in the Supplementary Material (Supplementary Text S1).

105

#### 3.1 Organic carbon isotope compositions

The carbon isotope compositions of organic matter in paleosol samples were analysed in the Stable Isotope Laboratory of the Institute of Earth Surface Dynamics, University of Lausanne (IDYST-UNIL). Samples first underwent de-carbonatation with 10 % v/v HCl, then thoroughly washed with deionized water and dried at 40 °C for 48 h. The  $\delta^{13}\text{C}_{\text{org}}$  measurements were made using a Carlo Erba 1100 (Fisons Instruments, Milan, Italy) elemental analyser connected to a Thermo Fisher Scientific Delta V Plus isotope ratio mass spectrometer, both operated under continuous helium flow. Measured  $\delta^{13}\text{C}$  values were calibrated and normalized using international reference materials and in-house standards [Spangenberg 2006, 2016] and reported in per mil (‰) vs. Vienna Pee Dee Belemnite limestone standard (VPDB). The precision of the  $\delta^{13}\text{C}_{\text{org}}$  values were better than 0.1 ‰.

110

115

#### 3.2 Carbonate isotope compositions

Carbon and oxygen isotope compositions ( $\delta^{13}\text{C}_{\text{carb}}$ ,  $\delta^{18}\text{O}_{\text{carb}}$ ) were determined in the Stable Isotope Laboratory, IDYST-UNIL. Bulk paleosol samples containing >10 wt.%  $\text{CaCO}_3$ , including carbonate samples, were analysed using a Thermo Fisher Scientific Gas Bench II carbonate preparation device connected to a Delta V Plus isotope ratio mass spectrometer according to a method adapted after Spötl and Vennemann (2003).  $\text{CO}_2$  gas was produced by reaction with 99 % orthophosphoric acid at 70 °C. The  $\delta^{13}\text{C}_{\text{carb}}$  and  $\delta^{18}\text{O}_{\text{carb}}$  values are reported in ‰ vs. VPDB. Replicate measurements of the international calcite standard NBS 19 (limestone,  $\delta^{13}\text{C} = +1.95$  ‰,  $\delta^{18}\text{O} = -2.19$

120



125 ‰) and an in-house standard (Carrara Marble,  $\delta^{13}\text{C} = +2.05$  ‰,  $\delta^{18}\text{O} = -1.70$  ‰) yielded an analytical precision of  $\pm 0.05$  ‰ for  $\delta^{13}\text{C}_{\text{carb}}$  and  $\pm 0.1$  ‰ for  $\delta^{18}\text{O}_{\text{carb}}$ .

### 3.3 Major elements

130  $\text{SiO}_2$ ,  $\text{Al}_2\text{O}_3$ ,  $\text{Fe}_2\text{O}_3$ ,  $\text{MnO}$ ,  $\text{MgO}$ ,  $\text{CaO}$ ,  $\text{Na}_2\text{O}$ ,  $\text{K}_2\text{O}$ ,  $\text{P}_2\text{O}_5$ ,  $\text{Cr}_2\text{O}_3$ ,  $\text{NiO}$ , and loss on ignition (LOI), were measured in the powdered bulk paleosol samples by X-ray fluorescence (XRF; Phillips PANalytical PW2400 spectrometer) at the Institute of Earth Sciences of the University of Lausanne (ISTE-UNIL). The analyses were performed on fused glass discs prepared with  $1.2000 \pm 0.0005$  g ignited sample powder and  $6.0000 \pm 0.0005$  g of lithium tetraborate ( $\text{Li}_2\text{B}_4\text{O}_7$ ). The concentrations of the major elements were expressed as wt.% oxides. The analytical precision ( $1 \sigma$ ) assessed by replicate analyzed of international reference materials is 0.4 %.

### 3.4 Weathering indices

135 The chemical index of alteration (CIA, %) defined by Nesbitt and Young (1982) was used to quantify the degree of weathering. CIA values were determined using the molar ratio of immobile  $\text{Al}_2\text{O}_3$  and the mobile oxides  $\text{CaO}_2$ ,  $\text{Na}_2\text{O}$ , and  $\text{K}_2\text{O}$  in the silicate fraction (details in Text S1).

### 3.5 Mean annual precipitation

140 Mean annual precipitation (MAP,  $\text{mm yr}^{-1}$ ) was calculated using the equation proposed by Sheldon et al. (2002) (Text S1). This approach is based on an empirical relationship between the CIA and MAP of modern soils, and while values are well-supported for soil types from different climatic settings, multiple proxies such as paleobotanical estimates must be used to confirm the results. Topography, chemical composition of parent material, diagenesis of older paleosols are some of the factors that may limit the application of this proxy [Sheldon et al., 2009].

### 145 3.6 Clumped ( $\Delta_47$ ) isotopes

Clumped isotope compositions were measured at the Stable Isotope Laboratory of IDYST-UNIL, using a Nu-Perspective dual-inlet mass spectrometer with an automated NuCarb sample preparation device. Carbonate digestion,  $\text{CO}_2$  purification procedure and measurements were adapted after Anderson et al. (2021). For  $\Delta_47$  analyses, 3.8 to 4.2 mg of carbonate were reacted at 70 °C with 110  $\mu\text{l}$  105 wt.% phosphoric acid ( $\text{H}_3\text{PO}_4$ ), and the liberated  $\text{CO}_2$  was purified after digestion in a series of temperature-controlled, liquid-nitrogen-cooled cold fingers, including an adsorption trap (packed with Porapak Q 50/80 mesh) held at -30 °C. We applied the acid fractionation factor of +0.088 ‰ (Anderson et al. 2021) to the data in order to compare with the ETH-standards reacted at 90 °C (Bernasconi et al., 2021).



155 Three standards (ETH-1, ETH-2, ETH-3) have been used to calibrate  $\Delta_{47}$  values of unknown samples using a  
linear regression with the respective  $\Delta_{47}$  values of 0.205, 0.209, and 0.613 (Bernasconi et al., 2021). Temperatures  
are calculated using the calibration of Anderson et al. (2021), where  $\Delta_{47}$  is in ‰ and T in °C, as:

$$\Delta_{47} = (0.0391 \pm 0.0004) \times (10^6/T^2) + (0.154 \pm 0.004)$$

### 3.7 Clay mineralogy

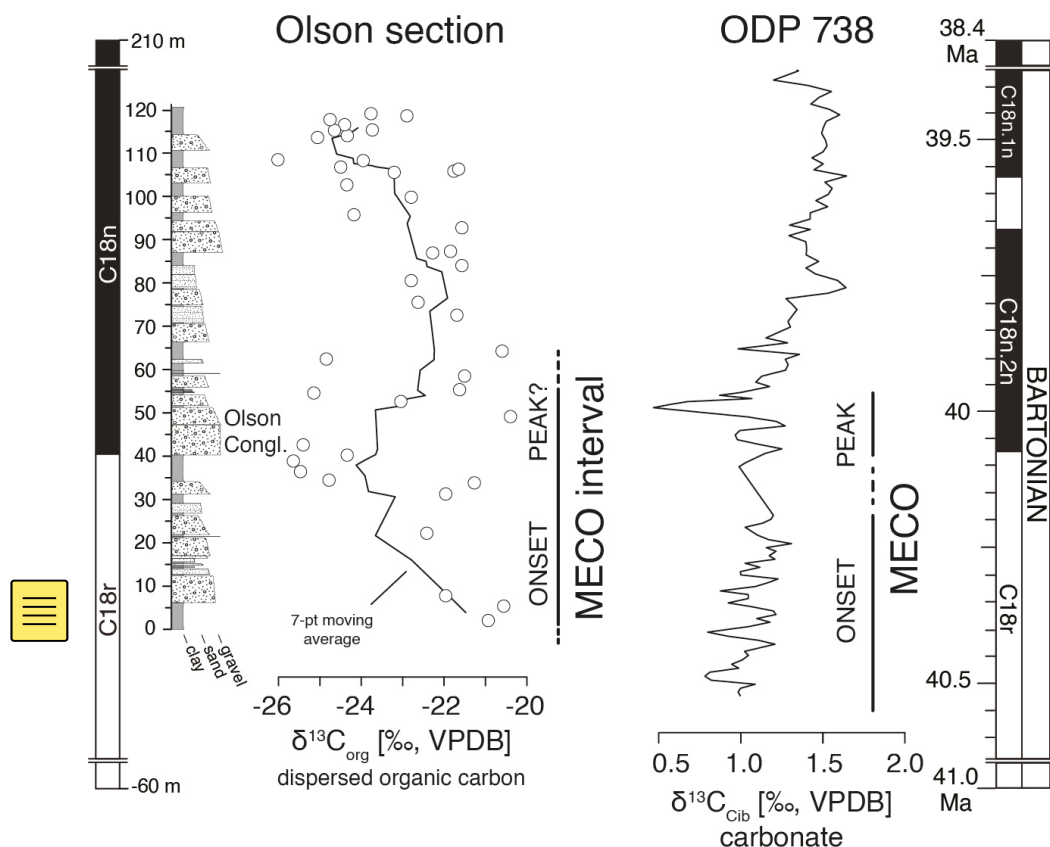
160 Clay mineralogical assemblages in paleosol samples were determined by X-ray diffractometry (XRD) at the ISTE-  
UNIL laboratories. Samples were prepared following the procedure described in Adatte et al. (1996). Analyses  
were made using a Thermo Fisher Scientific ARL X-TRA diffractometer and the intensities of the XRD peaks  
characteristic for each mineral, were used to estimate the relative percentage of clay minerals in the < 2  $\mu\text{m}$  and  
2–16  $\mu\text{m}$  size fractions.

## 165 4 Results and discussion

### 4.1 $\delta^{13}\text{C}$ of bulk paleosol organic matter

The  $\delta^{13}\text{C}_{\text{org}}$  values of the paleosols have a range between -26.0 and -20.4 ‰ with an average value of -23.2 ‰  
(Fig. 3). A negative CIE is marked by a 3 ‰ shift from the base of the section (from 0 to 30 m), where the onset  
begins, followed by a plateau of low values (30–50 m) that gradually return to higher values 60 m upwards. Such  
170 a large magnitude of the excursion in  $\delta^{13}\text{C}_{\text{org}}$  was previously identified for the PETM within the intermontane  
Piceance Creek Basin of western Colorado (USA), where a negative CIE of about 3 ‰ was reported [Foreman et  
al., 2012], while the  $\delta^{13}\text{C}_{\text{org}}$  record from the Middle Eocene Alano di Piave section deposited in the marginal  
Tethys Ocean showed a negative CIE of about 1 ‰ [Spofforth et al., 2010]. Nevertheless,  $\delta^{13}\text{C}_{\text{org}}$  patterns are  
similar to the trends observed in the benthic foraminiferal carbon stable isotope record ( $\delta^{13}\text{C}_{\text{cib}}$ ) from ODP sites  
175 738 (Fig. 3), indicating a general agreement in the change of  $\delta^{13}\text{C}$  values, even though absolute differences in the  
magnitude of excursions exist. The presence of a synchronous negative CIE therefore suggests that the MECO  
can be recognized in the continental Escanilla Fm.





180 Figure 3. Dispersed organic carbon isotope compositions ( $\delta^{13}\text{C}_{\text{org}}$ ) in paleosol samples (white circles) presented with a 7-point moving average for the change in benthic foraminiferal (genus *Cibicides*) carbon isotope record ( $\delta^{13}\text{C}_{\text{Cib}}$ ) from ODP site 738.

The  $\delta^{13}\text{C}_{\text{org}}$  values can also be used as indicators of paleoecology and paleoclimate [Kohn 2010].  $\text{C}_3$  plants which include trees, most shrubs and cool season grasses, have  $\delta^{13}\text{C}$  values generally between -37 ‰ and -20 ‰ and have dominated the history of terrestrial vegetation [Kohn 2010]. The wide range in  $\delta^{13}\text{C}$  values of plants is dependent on several factors including the mean annual precipitation (MAP) [Schulze et al. 1996; Kohn 2010]. Non water-stressed  $\text{C}_3$  plants are enriched in  $^{12}\text{C}$  and hence have more negative  $\delta^{13}\text{C}$  values, typically lower than -26 ‰. Higher  $\delta^{13}\text{C}$  values (> -26 ‰) are associated with plants growing under water deficient conditions and low soil transpiration rates (MAP < 500 mm yr<sup>-1</sup>) [e.g., Cerling and Quade 1993; Kohn 2010; Methner et al., 2016]. ~~At first sight,~~ the measured  $\delta^{13}\text{C}_{\text{org}}$  values point to a predominance of  $\text{C}_3$  vegetation, typical for an Eocene ecosystem [Cerling and Quade 1993; Methner et al., 2016]. They have relatively high  $\delta^{13}\text{C}$  values (about -23.2



‰) that are characteristic of dry environments with MAP < 500 mm yr<sup>-1</sup> [Kohn 2010]. The absence of a closed canopy forest, which would cause lower  $\delta^{13}\text{C}_{\text{org}}$  (< -31.5 ‰) due to the canopy effect [Kohn 2010], in the Escanilla Fm together with indications of dry conditions supports the presence of sparse vegetation in a dry and arid ecosystem.

Vegetation plays a key role in influencing landscape response to terrestrial hydroclimates during global warming events such as the PETM [Foreman et al., 2012]. For instance, de-vegetated fluvial banks enhance sediment erodibility, bank erosion, and lateral channel mobility, resulting in peak discharge and bedload sediment downstream flux even under a negligible increase in precipitation [Gran et al., 2001; Barefoot et al., 2021]. Sparse vegetation in the fluvial Escanilla Fm reflects the response of the Escanilla rivers to peak discharge and sediment flux events, which modified the stratigraphic architecture described as alternating sequences of high amalgamation (HA) and low amalgamation (LA) intervals [Sharma et al., 2023]. Such large flux in the Escanilla Fm at Olson during the MECO is also consistent with the clastic progradation event observed in the Jaca Basin [Peris Cabré et al., 2023], indicating the transmission and preservation of sedimentary flux signals in the sedimentary record from source-to-sink. Lastly, enhanced channel mobility during the MECO could also have lead to the export of large quantities of fine-grained (floodplain) sediment to the marine domain and potentially affected the carbonate environments developing at that time on the southern Margin of the Jaca-Pamplona trough (e.g. Garcès et al., 2023).

#### 210 4.2 $\delta^{13}\text{C}$ and $\delta^{18}\text{O}$ of bulk paleosol carbonates

The  $\delta^{13}\text{C}_{\text{carb}}$  values in paleosol bulk carbonates have a range from -2.6 to -1.0 ‰ with an average of -1.6 ‰ (Fig. 4). A transient decrease in  $\delta^{13}\text{C}_{\text{carb}}$  values is observed at 40 m where a negative CIE of about 1.0 ‰ magnitude is considered to represent the MECO negative CIE in the Escanilla Fm, followed by an increase in  $\delta^{13}\text{C}_{\text{carb}}$  values to -1.5 ‰ towards the top of the section (Fig. 4). These values are synchronous to the negative CIE recorded in paleosol organic matter, although a difference in magnitude is apparent. Such differences in magnitude do exist between CIE from different terrestrial archives [e.g., Gallagher et al., 2019]. For instance, the magnitude of negative CIE during the PETM is on average greater in paleosol carbonates by 2 ‰ than in preserved paleosol organic matter [Cotton et al., 2015; Gallagher et al., 2019]. However,  $\delta^{13}\text{C}$  records from the Escanilla Fm show a contrasting trend, likely indicating a difference in the soil carbon cycling between the MECO and the PETM, which requires further research. Additionally, the largest magnitude of excursion recorded by  $\delta^{13}\text{C}_{\text{org}}$  (Fig. 3)



perhaps also suggests that the organic carbon isotope record is a more sensitive proxy for the MECO, for reasons that are beyond the scope of this work.

$\delta^{13}\text{C}_{\text{carb}}$  values in carbonates (stromatolites and pedogenic nodules) have a range from -4.9 ‰ to -1.1 ‰ with an average value of -2.7 ‰. A negative trend 20 m onwards culminates just above the OC at 55 m and likely represents the MECO negative CIE in stromatolites and pedogenic nodule samples (Fig. 4). Further,  $\delta^{13}\text{C}_{\text{carb}}$  values from stromatolites and pedogenic nodules show a consistent 1 to 2 ‰ negative offset when compared to values from paleosol bulk carbonates which can be explained by the presence of detrital Mesozoic carbonates ( $\delta^{13}\text{C}_{\text{carb}} = 0$  ‰; Zamarreno et al., 1997) in the bulk sediments from the source area. Since bulk soil composition consists of both pedogenic and detrital components, we estimate 60 % pedogenic origin of the carbonates in the Escanilla paleosols assuming normal paleosol values of -1.5 ‰ and that stromatolites and pedogenic nodules represent endmembers having a  $\delta^{13}\text{C}_{\text{carb}}$  value of -2.5 ‰ (by simple mass balance where the bulk soil composition = pedogenic proportion × pedogenic composition + detrital proportion × detrital composition).

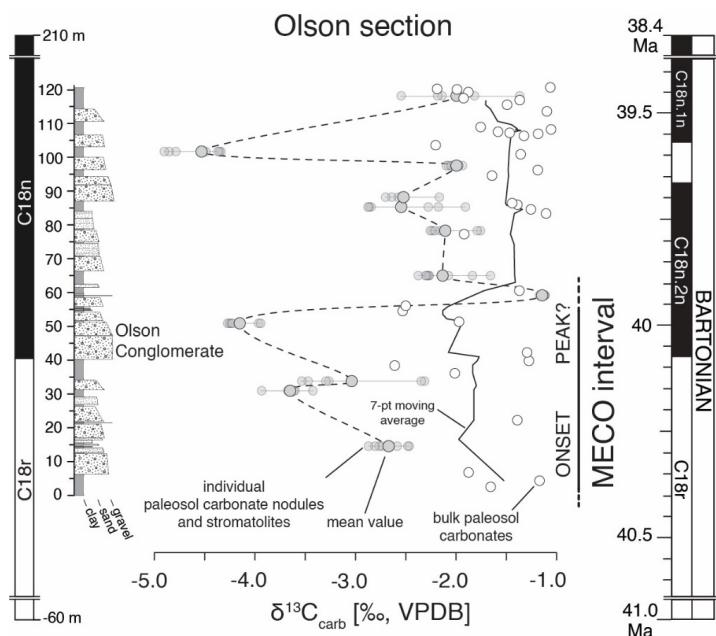
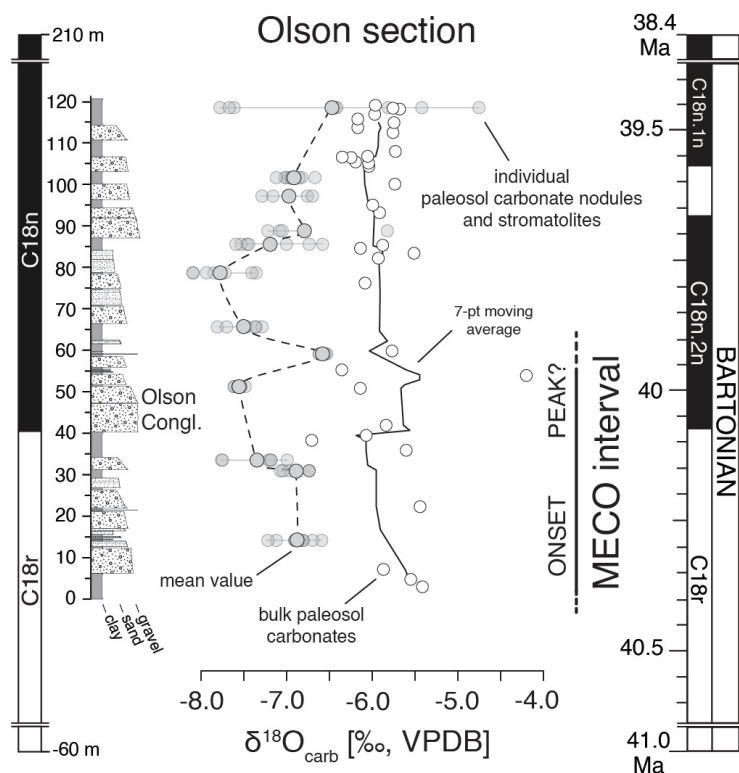


Figure 4. Carbon isotope compositions ( $\delta^{13}\text{C}_{\text{carb}}$ ) from paleosol bulk carbonates (white circles) with a 7-point moving average and from stromatolite and pedogenic nodules (grey circles) for the Olson section. Also marked is the MECO onset and peak interval based on  $\delta^{13}\text{C}_{\text{org}}$  values in this study.



The  $\delta^{18}\text{O}_{\text{carb}}$  values in paleosol bulk carbonates have a range between -6.7 and -4.2 ‰ with an average of -5.8 ‰ (Fig. 5). A positive OIE of about 0.5 ‰ magnitude, suggestive of an increase in freshwater  $^{18}\text{O}$  content and hence perhaps warming, occurs at the 40 to 60 m interval and likely represents peak MECO conditions in the Escanilla Fm. Peak warming also corresponds to the OC where highest discharge and flux estimates have been predicted [Sharma et al., 2023]. Following the positive OIE,  $\delta^{18}\text{O}_{\text{carb}}$  values decline and return to relatively stable values of around -6.0 ‰, 60 m onwards until the top of the Olson section, and may represent the post-MECO cooling phase (Fig. 5).

The  $\delta^{18}\text{O}_{\text{carb}}$  values in stromatolites and pedogenic nodules have a range from -8.1 to -4.7 ‰ with an average value of -7.1 ‰; they crudely match the  $\delta^{18}\text{O}$ -trend in paleosol bulk carbonates. An increase in  $\delta^{18}\text{O}_{\text{carb}}$  occurs above the OC at 60 m and most probably represent also the peak MECO warming (Fig. 4). A large spread in replicate measurements of some samples could be due to heterogeneities in carbonate composition within the same sample.



250 Figure 5. Oxygen isotope compositions ( $\delta^{18}\text{O}_{\text{carb}}$ ) from paleosol bulk carbonates (white circles) with a 7-point moving average, and carbonate samples (grey circles; stromatolites and pedogenic nodules) for the Olson section. Also marked is the MECO onset and peak interval based on  $\delta^{13}\text{C}_{\text{org}}$  values in this study.

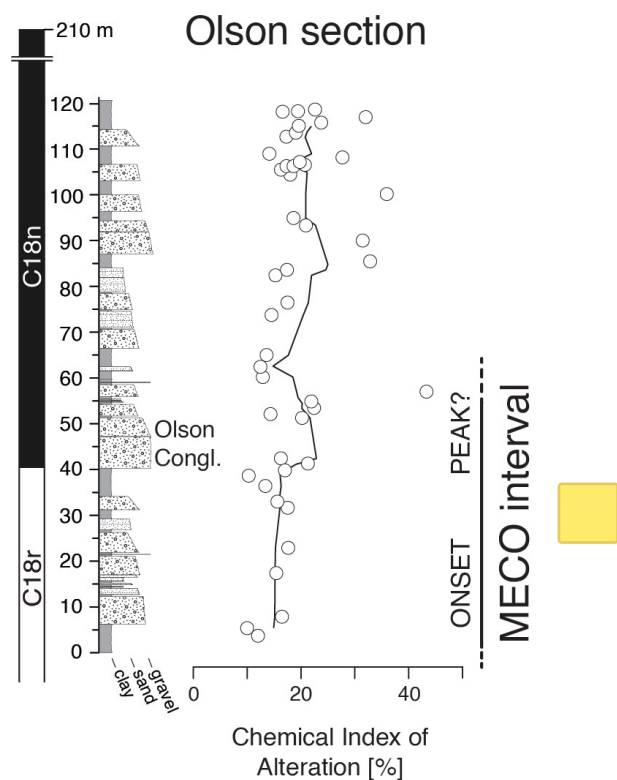


In summary, stable isotope data from the Escanilla Fm at Olson is compatible with climate perturbations through  
255 excursions similar to the isotope excursions in the marine records, even though there are differences in the  
magnitude of excursions. These excursions have also been identified downstream in the time-equivalent marine  
sediments in the Jaca Basin, Spain [Peris Cabré et al., 2023]. This indicates the preservation of MECO climate  
perturbation signals in the source-to-sink Escanilla sediment routing system. Furthermore, irrespective of the  
presence of authigenic and detrital carbonates in paleosol samples, the CIE of organic matter suggests that the  
260 MECO can be regionally recognized in the Escanilla Fm.

#### 4.3 Weathering conditions

CIA values vary between 9 and 43 % (average of 19 %) and remain almost constant throughout the section. A  
limited peak in CIA values may represent peak weathering conditions during the MECO (Fig. 6). However, such  
265 low values are broadly indicative of weak chemical weathering, and if true, suggest a prevalence of physical  
weathering and erosion during the Middle Eocene. This contrasts with the assumption of intense weathering trends  
during global warming and recently published results for earlier hyperthermals [Tanaka et al., 2022]. For instance,  
during the PETM, CIA values have been estimated to be in the 75–85 % range [Stokke et al., 2021]. These  
relatively low CIA values could be related to the long-term trend of low silicate weathering in response to elevated  
270 pCO<sub>2</sub> and warming levels during the Middle Eocene, as indicated by Os isotopes [van der Ploeg et al., 2018].  
Current understanding of the Earth's carbon cycle suggests strengthening of the negative silicate weathering  
feedback in response to rising atmospheric pCO<sub>2</sub> [Colbourn et al., 2015; Penman et al., 2020]. However, the  
strength of the feedback depends primarily on several local/regional environmental variables such as temperature  
and precipitation, in addition to geomorphology and lithology [e.g., Richey et al., 2020; Deng et al., 2022]. Our  
275 estimated weathering intensities could thus be indicative of a local dry and arid climate with a weakened  
hydrologic system in northern continental Spain during the Middle Eocene. Such low weathering rates, if  
confirmed at a scale relevant to the global carbon cycle, could also explain the sustained elevated carbon levels  
for a longer duration than during the previous hyperthermals, highlighting the different dynamics of the MECO  
[Sluijs et al., 2013; van der Ploeg et al., 2018].





280

Figure 6. Chemical index of alteration (CIA) values from paleosols (white circles) with a 7-point moving average to quantify weathering in the Escanilla Fm at Olson.

#### 4.4 Regional climate record during the Middle Eocene

##### 4.4.1 Mean annual precipitation (MAP) estimates

285

MAP values in the Olson section range from 270 to 570 mm yr<sup>-1</sup> with an average of 330 ± 182 mm yr<sup>-1</sup>. Values stay constant at 300 mm yr<sup>-1</sup> until 40 m followed by a small increase in precipitation up to about 370 mm yr<sup>-1</sup> that corresponds to the OC (peak MECO conditions), before returning to an average value of 340 mm yr<sup>-1</sup> until the top

290

of the section (Fig. 7). Overall, these values consistently predict arid (semi-arid) conditions in this area of the southern Pyrenees during the Middle Eocene and are coherent with the high  $\delta^{13}C_{org}$  values measured in our section and linked with water-stressed environments. In other localities of the Ebro Basin, in northeastern Spain, climate interpretations based on palynological, pollen taxa and floral diversity studies [Cavagnetto and Anadón 1996; Haseldonckx, 1972] suggest warm climate and humid vegetation, with preservation for instance of mangrove swamp vegetation along the coast. The absence of evidence of humid climate in Olson could be due to its inland



295 location, away from the coastline in a better drained floodplain setting. Such regional differences in climate could also be the result of a climate transition phase during the Middle Eocene, oscillating from a warm tropical Early Eocene to a cold and arid Early Oligocene, expressed differently in different regions and at possibly different sampled intervals.

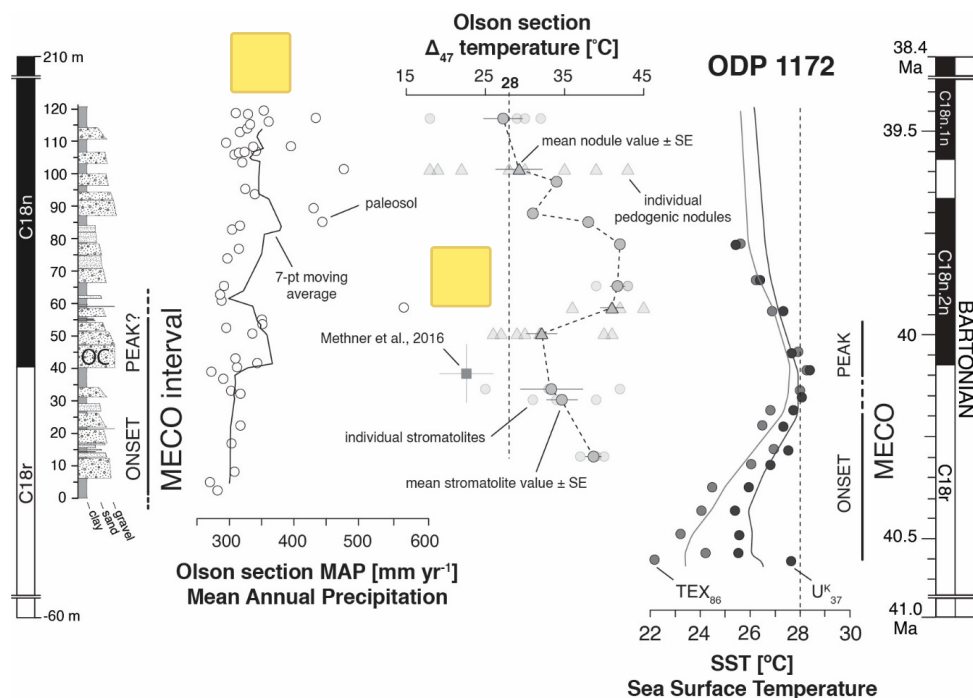
Interestingly, arid conditions, based on palynological analysis, have also been identified in the Xining Basin in

300 NW China at ~40 Ma [Bosboom et al., 2014]. However, this has been linked to post-MECO cooling rather than transient warming during the MECO. MAP estimates reported in this study are considerably lower when compared

to Middle Eocene contemporary bio-climate analysis of south-eastern Australian flora, which predict MAP values between 1530 and 2370 mm yr<sup>-1</sup>, consistent with modern rainforest climates [Greenwood et al., 2003], while MAP estimates from continental central Europe are in the range of 1100 to 1400 mm yr<sup>-1</sup> [Mosbrugger et al., 2005].

305 Other proxy data from southern France indicate a MAP less than 500 mm yr<sup>-1</sup> in the Bartonian [Kocsis et al., 2014], and is similar to our calculation from Spain. Our estimates are also comparable to modern-day MAP values of northern Spain, which range from 400 to 1000 mm yr<sup>-1</sup> [Hijmans et al., 2005; Huyghe et al., 2018]. Considering the high Ca content (> 20 wt.%) in sampled paleosols, our MAP values possibly underestimate true precipitation values due to an artificial reduction in the ratio of Al to other metals when calculating the chemical index of

310 weathering (CIW, Text S1) [Stein et al., 2015]. Nevertheless, this does not explain the regional disparities in precipitation regimes during the Middle Eocene, and values reported here should be regarded as representative of a local regional signal, most likely influenced by the ongoing Pyrenean orogeny and the resulting orographic (rainshadow) effects [Vacherat et al., 2017; Huyghe et al., 2018], similar to the modern situation.



315

Figure 7. Mean annual precipitation (MAP) values (white circles) from the Olson section are presented by a 7-point moving average, followed by clumped isotope ( $\Delta_{47}$ ) temperatures from stromatolites (grey circles) and pedogenic nodules (grey triangles). For each sample, individual values are presented along with the respective mean value  $\pm$  standard error (SE). We compare our terrestrial temperature estimates to sea surface temperatures ( $TEX_{86}$  and  $U^{K}_{37}$ ) having a 3-point moving average (Bijl et al., 2010).

320

#### 4.4.2 Carbonate clumped isotope thermometry

$\Delta_{47}$  values of carbonate in stromatolites have a range from 0.634 to 0.704 ‰, translating into temperatures of 18 to 43 °C (Fig. 7). Each stromatolite was analyzed 1 to 3 times for replicate measurements. Standard error for replicate measurements range from 0.006 to 0.011 ‰.  $\Delta_{47}$  values of carbonate in pedogenic nodules have a range from 0.629 to 0.704 ‰, translating into temperatures of 18 to 45 °C (Fig. 7). Each pedogenic nodule was analyzed 4 to 8 times for replicate measurements having standard error ranging from 0.006 to 0.009 ‰. It is, however, important to note that while measurement reproducibility was good, care must be taken while interpreting  $\Delta_{47}$  data as a number of potentially significant uncertainties are associated with it. For instance,  $\Delta_{47}$  temperatures may not necessarily reflect primary formation temperatures but could instead be the result of a combination of primary formation temperatures and secondary effects such as potential diagenetic temperatures that bias primary

330



compositions, although secondary overprinting is unlikely to produce cooler temperatures [Hren and Sheldon  
2019]. A ~~large(r)~~ spread recorded in a few samples could be likely due to inhomogeneity in the analyzed sample  
powder. Furthermore, peak temperatures are found only within 25 m of the Olson section without any change in  
335 lithology. In addition, a similar temperature range in both stromatolites and pedogenic nodules further suggests  
that analyzed samples most likely did not undergo significant diagenetic alteration after their formation.  
Mean temperatures vary from  $32.1 \pm 1.8$  °C to  $38.6 \pm 0.72$  °C in the lower half of the section until 50 m followed  
by an increase just above the OC with a maximum mean temperature of 42 °C at 80 m. 90 m upwards until the  
top of the section, values return to an average value of 30 °C. Available magnetostratigraphic age constrains for  
340 the Escanilla Fm and its linear correlation to the GPTS, allow the identification of a potential lag between marine  
and terrestrial MECO climate signals. Interestingly, recorded peak temperatures occur about 400 ~~km~~ after peak  
MECO warming in the marine realm, suggesting, if our estimates are correct, a significant lag of peak temperature  
on the continents with respect to oceans. Soil carbonates typically form during warm and dry periods and  
consequently have a strong summer seasonal bias in T ( $\Delta_{47}$ ) values [Quade et al., 2013; Burgener et al., 2016;  
345 Huth et al., 2019]. As a result,  $\Delta_{47}$  temperature from pedogenic nodules may be biased towards warm month mean  
temperatures (WMMT) and on average exceed mean annual temperatures by 10 to 15 °C [Quade et al., 2013].  
 $\Delta_{47}$  temperatures from the Escanilla Fm also suggest a land-sea temperature gradient of 5 to 10 °C when compared  
to different sea surface temperature (SST) records, that is from ODP site 1172 (Tasmania, Pacific; Bijl et al.,  
2010) and IODP sites U1408 and U1410 (northwest Atlantic Ocean; van der Ploeg et al., 2023) indicating an  
350 amplifying effect due to continentality and change in the season of carbonate growth. Similar continental  
temperature sensitivity was previously also identified through clumped temperatures of pedogenic carbonates in  
the continental interiors of SW Montana, USA [Methner et al., 2016].  
 $\Delta_{47}$  temperatures were further used to calculate the  $\delta^{18}\text{O}$  of fluids in equilibrium with carbonates using the  
temperature dependent fractionation factor of Epstein et al., (1953).  $\Delta_{47}$  temperatures and  $\delta^{18}\text{O}_{\text{carb}}$  values give  
355 water  $\delta^{18}\text{O}$  values of -6.5 to -0.8 ‰ (average of -3.5 ‰) for T = 25 °C (see Text S1), which although consistent  
with a range of fresh meteoric water at low latitude, are still on the higher end, most likely signifying  $^{18}\text{O}$ -isotope  
enrichment due to excess evapotranspiration under arid climatic conditions, consistent with estimates from other  
proxies used in this study.

#### 360 4.4.3 Clay mineralogy



Clay mineral assemblages in paleosols are also important paleoclimatic indicators and provide integrated records of the overall climate [Singer, 1984]. Smectite, palygorskite, illite, and chlorite form up to 98 % of the identified mineral assemblages in the studied section (Fig. S1; supplementary material). Smectite, which typically forms under seasonal rainfall conditions with a pronounced dry season [e.g., Singer, 1984; Tabor et al., 2014], constitutes on average 17 % of the total identified clay mineral assemblage while individual values range up to 58 %. Palygorskite often indicates an arid and semi-arid environment where evapotranspiration exceeds precipitation [e.g., Birkeland, 1984; Singer, 2002; Meunier, 2005], and constitutes up to 25 % (average of 10 %) of the total clay mineral assemblage. The presence of palygorskite together with smectite suggests a hot climate with some rain intervals [Xie et al., 2013; Luiz da Silva et al., 2018] and thus corroborates our low MAP and clumped isotope temperature values. Illite content is between 11 and 53 % (average of 36 %) while chlorite content is between 7 to 64 % (average of 35 %) in the analyzed paleosols. High amounts of illite and chlorite are typically found in sediments formed by physical weathering and are thus indicative of weak, incipient chemical weathering [Tabor et al., 2014], and support our calculated CIA values.

## 375 5 Conclusions

Detailed geochemical and mineralogical analysis of paleosols, stromatolites, and pedogenic nodules, provide new insights into terrestrial records of the MECO in the Ainsa Basin of the southern Pyrenees, Spain. A negative CIE measured for organic matter indicates that the MECO is recognized in the fluvial Escanilla Fm, further supported by the presence of carbon and oxygen isotope excursions in whole rock carbonates, nodules and stromatolites, demonstrating that continental sedimentary successions can also serve as climate archives, and highlighting stable isotope proxies as a powerful dating and correlation tool in notably difficult to date fluvial successions. Low CIA values in the Escanilla Formation suggest a poor silicate weathering feedback to elevated CO<sub>2</sub> levels and a prevalence of physical erosion during the Middle Eocene. This is compatible with an arid climate, i.e., a locally diminished hydrological cycle, supported by MAP estimates and clay mineral assemblages in the fluvial sedimentary succession. Carbonate clumped isotope thermometry suggests high temperatures with a possible ~ 400 Kyr lag in peak temperatures with respect to the MECO timing in the oceanic domain, and an amplifying effect of 10 to 15 °C (for summer temperatures) on continents compared to temperature records from the deep-sea.

## 390 References





- Adatte, T., Stinnesbeck, W., and Keller, G., 1996. Lithostratigraphic and mineralogic correlations of near K/T boundary clastic sediments in northeastern Mexico: implications for origin and nature of deposition. *Spec. Pap. Geol. Soc. Am.*, 307:211–226.
- Anderson, N.T., Kelson, J.R., Kele, S., Daëron, M., Bonifacie, M., Horita, J., Mackey, T.J., John, C.M., Kluge, T., Petschnig, P., Jost, A.B., Huntington, K.W., Bernasconi, S.M., Bergmann, K.D., 2021. A Unified clumped isotope thermometer calibration (0.5–1,100°C) using carbonate-based standardization. *Geophys Res Lett* 48. <https://doi.org/10.1029/2020gl092069>
- Barefoot, E.A., Nittrouer, J.A., Foreman, B.Z., Hajek, E.A., Dickens, G.R., Baisden, T., Toms, L., 2021. Evidence for enhanced fluvial channel mobility and fine sediment export due to precipitation seasonality during the Paleocene-Eocene thermal maximum. *Geology*. <https://doi.org/10.1130/g49149.1>
- Bernasconi, S.M., Daëron, M., Bergmann, K.D., Bonifacie, M., Meckler, A.N., Affek, H.P., Anderson, N., Bajnai, D., Barkan, E., Beverly, E., Blamart, D., Burgener, L., Calmels, D., Chaduteau, C., Clog, M., Davidheiser-Kroll, B., Davies, A., Dux, F., Eiler, J., Elliott, B., Fetrow, A.C., Fiebig, J., Goldberg, S., Herosmo, M., Huntington, K.W., Hyland, E., Ingalls, M., Jaggi, M., John, C.M., Jost, A.B., Katz, S., Kelson, J., Kluge, T., Kocken, I.J., Laskar, A., Leutert, T.J., Liang, D., Lucarelli, J., Mackey, T.J., Mangenot, X., Meinicke, N., Modestou, S.E., Müller, I.A., Murray, S., Neary, A., Packard, N., Passey, B.H., Pelletier, E., Petersen, S., Piasecki, A., Schauer, A., Snell, K.E., Swart, P.K., Tripathi, A., Upadhyay, D., Vennemann, T., Winkelstern, I., Yarian, D., Yoshida, N., Zhang, N., Ziegler, M., 2021. InterCarb: A Community Effort to improve interlaboratory standardization of the carbonate clumped isotope thermometer using carbonate standards. *Geochem Geophys Geosystems* 22, e2020GC009588. <https://doi.org/10.1029/2020gc009588>
- Bijl, P.K., Houben, A.J.P., Schouten, S., Bohaty, S.M., Sluijs, A., Reichert, G.-J., Damsté, J.S.S., Brinkhuis, H., 2010. Transient Middle Eocene atmospheric CO<sub>2</sub> and temperature variations. *Science* 330, 819–821. <https://doi.org/10.1126/science.1193654>
- Birkeland, P.W., 1984. *Soils and geomorphology*. Oxford university press.
- Bohaty, S.M., Zachos, J.C., Florindo, F., Delaney, M.L., 2009. Coupled greenhouse warming and deep-sea acidification in the middle Eocene. *Paleoceanography* 24, PA2207. <https://doi.org/10.1029/2008pa001676>
- Bosboom, R.E., Abels, H.A., Hoorn, C., Berg, B.C.J. van den, Guo, Z., Dupont-Nivet, G., 2014. Aridification in continental Asia after the Middle Eocene Climatic Optimum (MECO). *Earth Planet Sc Lett* 389, 34–42. <https://doi.org/10.1016/j.epsl.2013.12.014>



- 420 Burgener, L., Huntington, K.W., Hoke, G.D., Schauer, A., Ringham, M.C., Latorre, C., Díaz, F.P., 2016. Variations in soil carbonate formation and seasonal bias over >4 km of relief in the western Andes (30°S) revealed by clumped isotope thermometry. *Earth Planet Sc Lett* 441, 188–199. <https://doi.org/10.1016/j.epsl.2016.02.033>
- Cavagnetto, C., Anadón, P., 1996. Preliminary palynological data on floristic and climatic changes during  
425 the Middle Eocene-Early Oligocene of the eastern Ebro Basin, northeast Spain. *Rev Palaeobot Palyno* 92, 281–305. [https://doi.org/10.1016/0034-6667\(95\)00096-8](https://doi.org/10.1016/0034-6667(95)00096-8)
- Cerling, T.E., Quade, J., 1993. Stable carbon and oxygen isotopes in soil carbonates, in: P.K. Swart, K.C. Lohmann, J. McKenzie, S. Savin (Eds.), *Climate Change in Continental Isotopic Records*, Geophysical Monograph, vol. 78, AGU, pp. 217 – 231.
- 430 Colbourn, G., Ridgwell, A., Lenton, T.M., 2015. The time scale of the silicate weathering negative feedback on atmospheric CO<sub>2</sub>. *Global Biogeochem Cy* 29, 583–596. <https://doi.org/10.1002/2014gb005054>
- Cotton, J.M., Sheldon, N.D., Hren, M.T., Gallagher, T.M., 2015. Positive feedback drives carbon release from soils to atmosphere during Paleocene/Eocene warming. *Am J Sci* 315, 337–361. <https://doi.org/10.2475/04.2015.03>
- 435 Deng, K., Yang, S., Guo, Y., 2022. A global temperature control of silicate weathering intensity. *Nat Commun* 13, 1781. <https://doi.org/10.1038/s41467-022-29415-0>
- Dreyer, T., Fält, L.-M., Høy, T., Knarud, R., Steel, R. and Cuevas, J.-L., 1992. Sedimentary Architecture of Field Analogues for Reservoir Information (SAFARI): A Case Study of the Fluvial Escanilla Formation, Spanish Pyrenees. In *The Geological modelling of hydrocarbon reservoirs and outcrop analogues* (eds S.S. Flint and I.D. Bryant). <https://doi.org/10.1002/9781444303957.ch3>
- 440 Epstein, S., Buchsbaum, R., Lowenstam, H.A. and Urey, H.C., 1953. Revised carbonate-water isotopic temperature scale. *GSA Bulletin* 64, 1315–1326. [https://doi.org/10.1130/0016-7606\(1953\)64\[1315:RCITS\]2.0.CO;2](https://doi.org/10.1130/0016-7606(1953)64[1315:RCITS]2.0.CO;2)
- Foreman, B.Z., Heller, P.L., Clementz, M.T., 2012. Fluvial response to abrupt global warming at the  
445 Palaeocene/Eocene boundary. *Nature* 491, 92–95. <https://doi.org/10.1038/nature11513>
- Gallagher, T.M., Cacciatore, C.G., Breecker, D.O., 2019. Interpreting the Difference in Magnitudes of PETM Carbon isotope excursions in paleosol carbonate and organic matter: Oxidation of methane in soils versus elevated soil respiration rates. *Paleoceanogr Paleoclimatology* 34, 2113–2128. <https://doi.org/10.1029/2019pa003596>



- 450 Gran, K., Paola, C., 2001. Riparian vegetation controls on braided stream dynamics. *Water Resour Res* 37, 3275–3283. <https://doi.org/10.1029/2000wr000203>
- Greenwood, D.R., Moss, P.T., Rowett, A.I., Vadala, A.J., and Keefe, R.L., 2003, Plant communities and climate change in south- eastern Australia during the early Paleogene: in Wing, S.L., Gingerich, P.D., Schmitz, B., and Thomas, E., eds., *Causes and Consequences of Globally Warm Climates in the Early*
- 455 *Paleogene: Geological Society of America Special Paper* 369, p. 365–380.
- Haseldonckx, P., 1972. The presence of *Nypa* palms in Europe: a solved problem. *Geol.*
- Henehan, M.J., Edgar, K.M., Foster, G.L., Penman, D.E., Hull, P.M., Greenop, R., Anagnostou, E., Pearson, P.N., 2020. Revisiting the Middle Eocene Climatic Optimum “carbon cycle conundrum” with new estimates of atmospheric pCO<sub>2</sub> from boron isotopes. *Paleoceanogr Paleoclimatology* 35.
- 460 <https://doi.org/10.1029/2019pa003713>
- Hijmans, R.J., Cameron, S.E., Parra, J.L., Jones, P.G., Jarvis, A., 2005. Very high resolution interpolated climate surfaces for global land areas. *Int J Climatol* 25, 1965–1978. <https://doi.org/10.1002/joc.1276>
- Hren, M.T., Sheldon, N.D., 2020. Terrestrial microbialites provide constraints on the mesoproterozoic atmosphere. *Depositional Rec* 6, 4–20. <https://doi.org/10.1002/dep2.79>
- 465 Huth, T.E., Cerling, T.E., Marchetti, D.W., Bowling, D.R., Ellwein, A.L., Passey, B.H., 2019. Seasonal bias in soil carbonate formation and its implications for interpreting high-resolution paleoarchives: evidence from southern Utah. *J Geophys Res Biogeosciences* 124, 616–632. <https://doi.org/10.1029/2018jg004496>
- Huyghe, D., Mouthereau, F., Sébilo, M., Vacherat, A., Ségalen, L., Richard, P., Biron, P., Bariac, T., 2018. Impact of topography, climate and moisture sources on isotopic composition ( $\delta^{18}\text{O}$  &  $\delta\text{D}$ ) of rivers in the
- 470 Pyrenees: Implications for topographic reconstructions in small orogens. *Earth Planet Sc Lett* 484, 370–384. <https://doi.org/10.1016/j.epsl.2017.12.035>
- Jovane, L., Florindo, F., Coccioni, R., Dinarès-Turell, J., Marsili, A., Monechi, S., Roberts, A.P., Sprovieri, M., 2007. The middle Eocene climatic optimum event in the Contessa Highway section, Umbrian Apennines, Italy. *Gsa Bulletin* 119, 413–427. <https://doi.org/10.1130/b25917.1>
- 475 Kocsis, L., Ozsvárt, P., Becker, D., Ziegler, R., Scherler, L., Codrea, V., 2014. Orogeny forced terrestrial climate variation during the late Eocene–early Oligocene in Europe. *Geology* 42, 727–730. <https://doi.org/10.1130/g35673.1>
- Kohn, M.J., 2010. Carbon isotope compositions of terrestrial C<sub>3</sub> plants as indicators of (paleo)ecology and (paleo)climate. *Proc National Acad Sci* 107, 19691–19695. <https://doi.org/10.1073/pnas.1004933107>



- 480      Labourdette, R., Jones, R.R., 2007. Characterization of fluvial architectural elements using a three-dimensional outcrop data set: Escanilla braided system, South-Central Pyrenees, Spain. *Geosphere* 3, 422–434. <https://doi.org/10.1130/ges00087.1>
- Methner, K., Mulch, A., Fiebig, J., Wacker, U., Gerdes, A., Graham, S.A., Chamberlain, C.P., 2016. Rapid Middle Eocene temperature change in western North America. *Earth Planet Sc Lett* 450, 132–139. <https://doi.org/10.1016/j.epsl.2016.05.053>
- 485      Meunier, A., 2005. Clays in sedimentary environments. *Clays*, pp.295-327. *Mijnb.* 51, 645–650.
- Mosbrugger, V., Utescher, T., Dilcher, D.L., 2005. Cenozoic continental climatic evolution of Central Europe. *P Natl Acad Sci Usa* 102, 14964–14969. <https://doi.org/10.1073/pnas.0505267102>
- 490      Mulch, A., Chamberlain, C.P., Cosca, M.A., Teyssier, C., Methner, K., Hren, M.T., Graham, S.A., 2015. Rapid change in high-elevation precipitation patterns of western North America during the Middle Eocene Climatic Optimum (MECO). *Am J Sci* 315, 317–336. <https://doi.org/10.2475/04.2015.02>
- Nesbitt, H.W., Young, G.M., 1982. Early Proterozoic climates and plate motions inferred from major element chemistry of lutites. *Nature* 299, 715–717. <https://doi.org/10.1038/299715a0>
- 495      Ogg, J.G., 2020. Geologic Time Scale 2020 159–192. <https://doi.org/10.1016/b978-0-12-824360-2.00005-x>
- Pearson, P.N., Dongen, B.E. van, Nicholas, C.J., Pancost, R.D., Schouten, S., Singano, J.M., Wade, B.S., 2007. Stable warm tropical climate through the Eocene Epoch. *Geology* 35, 211–214. <https://doi.org/10.1130/g23175a.1>
- Penman, D.E., Rugenstein, J.K.C., Ibarra, D.E., Winnick, M.J., 2020. Silicate weathering as a feedback and forcing in Earth’s climate and carbon cycle. *Earth-sci Rev* 209, 103298. <https://doi.org/10.1016/j.earscirev.2020.103298>
- 500      Peris Cabré, S., Valero, L., Spangenberg, J. E., Vinyoles, A., Verité, J., Adatte, T., Tremblin, M., Watkins, S., Sharma, N., Garcés, M., Puigdefàbregas, C., and Castellort, S., 2023. Fluvio-deltaic record of increased sediment transport during the Middle Eocene Climatic Optimum (MECO), Southern Pyrenees, Spain. *Clim. Past*, 19, 533–554, <https://doi.org/10.5194/cp-19-533-2023>.
- 505      Ploeg, R. van der, Cramwinckel, M.J., Kocken, I.J., Leutert, T.J., Bohaty, S.M., Fokkema, C.D., Hull, P.M., Meckler, A.N., Middelburg, J.J., Müller, I.A., Penman, D.E., Peterse, F., Reichart, G.-J., Sexton, P.F., Vahlenkamp, M., Vleeschouwer, D.D., Wilson, P.A., Ziegler, M., Sluijs, A., 2023. North Atlantic surface



- ocean warming and salinization in response to middle Eocene greenhouse warming. *Sci Adv* 9, eabq0110.
- 510 <https://doi.org/10.1126/sciadv.abq0110>
- Ploeg, R. van der, Selby, D., Cramwinckel, M.J., Li, Y., Bohaty, S.M., Middelburg, J.J., Sluijs, A., 2018. Middle Eocene greenhouse warming facilitated by diminished weathering feedback. *Nat Commun* 9, 2877. <https://doi.org/10.1038/s41467-018-05104-9>
- Quade, J., Eiler, J., Daëron, M., Achyuthan, H., 2013. The clumped isotope geothermometer in soil and paleosol carbonate. *Geochim Cosmochim Acta* 105, 92–107. <https://doi.org/10.1016/j.gca.2012.11.031>
- 515 Richey, J.D., Montañez, I.P., Goddérís, Y., Looy, C.V., Griffis, N.P., DiMichele, W.A., 2020. Influence of temporally varying weatherability on CO<sub>2</sub>-climate coupling and ecosystem change in the late Paleozoic. *Clim Past* 16, 1759–1775. <https://doi.org/10.5194/cp-16-1759-2020>
- Schulze, E.-D., Ellis, R., Schulze, W., Trimborn, P., Ziegler, H., 1996. Diversity, metabolic types and  $\delta^{13}\text{C}$  carbon isotope ratios in the grass flora of Namibia in relation to growth form, precipitation and habitat conditions. *Oecologia* 106, 352–369. <https://doi.org/10.1007/bf00334563>
- 520 Sharma, N., Whittaker, A.C., Watkins, S.E., Valero, L., Vérité, J., Puigdefabregas, C., Adatte, T., Garcés, M., Guillocheau, F., Castellort, S., 2023. Water discharge variations control fluvial stratigraphic architecture in the Middle Eocene Escanilla Formation, Spain. *Sci Rep* 13, 6834. <https://doi.org/10.1038/s41598-023-33600-6>
- 525 Sheldon, N.D., Retallack, G.J., Tanaka, S., 2002. Geochemical climofunctions from north American soils and application to paleosols across the Eocene-Oligocene Boundary in Oregon. *J Geology* 110, 687–696. <https://doi.org/10.1086/342865>
- Sheldon, N.D., Tabor, N.J., 2009. Quantitative paleoenvironmental and paleoclimatic reconstruction using paleosols. *Earth-sci Rev* 95, 1–52. <https://doi.org/10.1016/j.earscirev.2009.03.004>
- 530 Silva, M.L. da, Batezelli, A., Ladeira, F.S.B., 2018. Genesis and paleoclimatic significance of palygorskite in the cretaceous paleosols of the Bauru Basin, Brazil. *Catena* 168, 110–128. <https://doi.org/10.1016/j.catena.2017.12.031>
- Singer, A., 1984. The paleoclimatic interpretation of clay minerals in sediments — a review. *Earth-sci Rev* 21, 251–293. [https://doi.org/10.1016/0012-8252\(84\)90055-2](https://doi.org/10.1016/0012-8252(84)90055-2)
- 535 Singer, A., 2002. Palygorskite and Sepiolite. In *Soil Mineralogy with Environmental Applications* (eds J.B. Dixon and D.G. Schulze). <https://doi.org/10.2136/sssabookser7.c18>





- Sluijs, A., Zeebe, R.E., Bijl, P.K., Bohaty, S.M., 2013. A middle Eocene carbon cycle conundrum. *Nat Geosci* 6, 429–434. <https://doi.org/10.1038/ngeo1807>
- 540 Spangenberg, J.E., 2006. Carbon and oxygen isotope working standards from C3 and C4 photosynthates. *Isot Environ Heat S* 42, 231–238. <https://doi.org/10.1080/10256010600841059>
- Spangenberg, J.E., 2016. Bulk C, H, O, and fatty acid C stable isotope analyses for purity assessment of vegetable oils from the southern and northern hemispheres. *Rapid Commun Mass Sp* 30, 2447–2461. <https://doi.org/10.1002/rcm.7734>
- 545 Spofforth, D.J.A., Agnini, C., Pälke, H., Rio, D., Fornaciari, E., Giusberti, L., Luciani, V., Lanci, L., Muttoni, G., 2010. Organic carbon burial following the middle Eocene climatic optimum in the central western Tethys. *Paleoceanography* 25. <https://doi.org/10.1029/2009pa001738>
- Spötl, C., Vennemann, T.W., 2003. Continuous-flow isotope ratio mass spectrometric analysis of carbonate minerals. *Rapid Commun. Mass Spectrom.* 17, 1004–1006. <https://doi.org/10.1002/rcm.1010>
- 550 Stein, R.A., Sheldon, N.D., Allen, S.E., Smith, M.E., Dzombak, R.M., Jicha, B.R., 2021. Climate and ecology in the Rocky Mountain interior after the early Eocene Climatic Optimum. *Clim Past* 17, 2515–2536. <https://doi.org/10.5194/cp-17-2515-2021>
- Stokke, E.W., Jones, M.T., Riber, L., Haflidason, H., Midtkandal, I., Schultz, B.P., Svensen, H.H., 2021. Rapid and sustained environmental responses to global warming: the Paleocene–Eocene Thermal Maximum in the eastern North Sea. *Clim Past* 17, 1989–2013. <https://doi.org/10.5194/cp-17-1989-2021>
- 555 Tabor, N.J., Myers, T.S., 2014. Paleosols as indicators of paleoenvironment and paleoclimate. *Annu Rev Earth Pl Sc* 43, 1–29. <https://doi.org/10.1146/annurev-earth-060614-105355>
- Tanaka, E., Yasukawa, K., Ohta, J., Kato, Y., 2022. Enhanced continental chemical weathering during the multiple early Eocene hyperthermals: New constraints from the southern Indian Ocean. *Geochim Cosmochim Ac* 331, 192–211. <https://doi.org/10.1016/j.gca.2022.05.022>
- 560 Vacherat, A., Mouthereau, F., Pik, R., Huyghe, D., Paquette, J.-L., Christophoul, F., Loget, N., Tibari, B., 2017. Rift-to-collision sediment routing in the Pyrenees: A synthesis from sedimentological, geochronological and kinematic constraints. *Earth-sci Rev* 172, 43–74. <https://doi.org/10.1016/j.earscirev.2017.07.004>
- 565 Villalba-Breva, Sheila & Martín-Closas, Carles & Marmi, Josep & Gomez, Bernard & Fernández-Marrón, Maria., 2012. Peat-forming plants in the Maastrichtian coals of the Eastern Pyrenees. *Geologica Acta*. 10. 189-207. 10.1344/105.000001711.



- Vinyoles, A., López-Blanco, M., Garcés, M., Arbués, P., Valero, L., Beamud, E., Oliva-Urcia, B., Cabello, P., 2020. 10 Myr evolution of sedimentation rates in a deep marine to non-marine foreland basin system: Tectonic and sedimentary controls (Eocene, Tremp–Jaca Basin, Southern Pyrenees, NE Spain). *Basin Res.* <https://doi.org/10.1111/bre.12481>
- 570
- Xie, Q., Chen, T., Zhou, H., Xu, X., Xu, H., Ji, J., Lu, H., Balsam, W., 2013. Mechanism of palygorskite formation in the Red Clay Formation on the Chinese Loess Plateau, northwest China. *Geoderma* 192, 39–49. <https://doi.org/10.1016/j.geoderma.2012.07.021>
- 575
- Zamarreño, I., Anadón, P., Utrilla, R., 1997. Sedimentology and isotopic composition of Upper Palaeocene to Eocene non-marine stromatolites, eastern Ebro Basin, NE Spain. *Sedimentology* 44, 159–176. <https://doi.org/10.1111/j.1365-3091.1997.tb00430.x>

#### **Acknowledgements**

We acknowledge support from the Swiss National Science Foundation (SNSF) for grant 200020\_182017: Earth Surface Signaling Systems 2 to Sébastien Castellort.

580

#### **Author contributions**

NS led fieldwork, sample preparation, data interpretation, and writing. JES performed stable-isotope analyses, data interpretation, discussion and writing. TA performed XRD analyses, data interpretation, and discussion. TV and LK performed clumped isotope analyses, and contributed to the discussion and editing. JV and LV contributed to fieldwork, review and editing. SC conceptualized and supervised the projet, acquired funding, contributed to the interpretation and writing.

585

#### **Competing interests**

The authors declare no competing interests.

#### **Data availability**

590 All data from this study are provided within the manuscript and its Supplementary Material.